American Mineralogist, Volume 89, pages 654–662, 2004

Quantitative electron microprobe analysis of $Fe^{3+}/\Sigma Fe$: Basic concepts and experimental protocol for glasses

MICHEL FIALIN,[1,2,*] ANTOINE BÉZOS,[2] CHRISTIANE WAGNER,[3] VÉRONIQUE MAGNIEN,[4] AND ERIC HUMLER[2]

[1]Centre de Microanalyse Camparis, Université Paris 6, 4 place jussieu, 75252 Paris cedex 5, France
[2]Laboratoire de Géosciences Marines, UMR 7097-CNRS, Université Paris 6 et 7, Institut de Physique de Globe, 4 place Jussieu, 75252 Paris cedex 5, France
[3]Laboratoire de Pétrologie, Modélisation des Matériaux et Processus, Université Paris 6, 4 place Jussieu, 75252 Paris cedex 5, France
[4]IPGP, 4 place Jussieu, 75252 Paris cedex 5, France

ABSTRACT

The presence of an unfilled 3d electron shell in the transition metals of the first series is manifested in X-ray self-absorption effects that cause distortions in the *L* emission spectra. In particular, one observes peak shape changes and peak position shifts toward lower energies that are attributed to X-ray photon self-absorption in the specimen. Self-absorption corresponds to partial overlap of both *L*-emission and absorption transitions in the region of the Fermi level. Such an overlap is related to relaxation effects that follow the creation of the core hole in the studied ions. For Fe, the overlap between the Fe$L\alpha$ emission peak and the corresponding FeL_{III} absorption band is clearly higher for Fe^{2+} than for Fe^{3+}, leading to an enhanced self-absorption induced shift of the Fe$L\alpha$ peak for Fe^{2+}. The shift of the $L\alpha$ peak between Fe^{2+} and Fe^{3+} can be measured with the electron microprobe and hence exploited to determine the $Fe^{3+}/\Sigma Fe$ ratios in silicates and glasses. For that purpose, an empirical method has been established based on working curves constructed from reference materials. A complete set of working curves is presented for glasses as well as an original experimental protocol.

Most glasses are electron beam sensitive and suffer especially from beam-induced oxidation-reduction mechanisms that are related to the implanted charge. The flux of Na^+ ions from the surface the depth in the glass (driven by the electric field induced by the electrostatic charge) tends to oxidize the surface whereas, concurrently, the counterflux of electrons produced by excitonic mechanisms and trapped at Fe^{3+} sites tends to reduce the surface. Therefore operating conditions should be set to minimize these phenomena, as they are a source of large discrepancies in $Fe^{3+}/\Sigma Fe$. The application of the current protocol gives uncertainties of about ±5% absolute for specimens with nominal total Fe concentrations ranging from 6 to 9 wt% (accuracy and precision on $Fe^{3+}/\Sigma Fe$ dramatically depend on the total Fe wt% concentration). Results obtained from a suite of basaltic glasses exhibit errors higher than ±5% absolute. Improved performances are expected for the method after the method can be used with promising new high resolution and high sensibility X-ray optics.

INTRODUCTION

Over the past few years, two major methods have been used to study the distribution and the local coordination environment of Fe^{2+} and Fe^{3+} ions in solids at the micrometer or sub-micrometer scale: (1) X-ray absorption spectroscopy (XAS) with synchrotron light sources (especially those of second- and third-generation with high-flux beamlines and high energy resolution) (e.g., Petit et al. 2001) and (2) electron energy loss spectroscopy (EELS) with a transmission electron microscope (offering high spatial resolution at the nanometer scale) (van Aken et al. 1998, 1999). For XAS and EELS, the methodology consists first of probing the absorption jump on either side of the Fe-*K* edge [1s → conduction band (CB) electronic transitions], or the Fe-$L_{2,3}$ edge (2p → CB), or the Fe-$M_{2,3}$ edge (3p → CB), and then of processing the experimental absorption to extract the information from both Fe^{2+} and Fe^{3+} components. Iron exhibits unfilled 3d states ($3d^5$ for Fe^{3+} and $3d^6$ for Fe^{2+}, to be compared to $3d^{10}$ for the filled level) that are located just above the Fermi level (e.g., Amthauer 1996). These empty 3d-states have a pronounced localized (or atomic) character, which produces large cross sections for the dipolar transitions (2p → 3d and 3p → 3d) and subsequent intense resonant peak-shaped absorption spectra. The number as well as the height and the position in energy of these pre-edge peaks (also known as XANES for X-ray absorption near edge structures with XAS, and ELNES for electron energy loss near edge structures with EELS) reflect the oxidation state and the local coordination environment of Fe. The $Fe^{3+}/\Sigma Fe$ ratios can be quantified by comparison of experimental and theoretical $L_{2,3}$- and $M_{2,3}$-XANES/ELNES spectra. Experimental profiles, representing different oxidation ratios, can be simulated by summation of the calculated multiplet structures of d^5 Fe^{3+} and d^6 Fe^{2+} (Cressey et al. 1993; Henderson et al. 1995). This approach can determine the $Fe^{3+}/\Sigma Fe$ ratios only approximately because theory still fails to interpret with accuracy the experimental spectra composed of a great number of multiplet lines (e.g., deGroot et al.

* E-mail: fialin@ccr.jussieu.fr

1990). Another method consists of processing the experimental spectra by multiple, linear, least-squares fitting methods using reference spectra collected from Fe^{2+}- and Fe^{3+}-bearing minerals (Garvie and Buseck 1998). However, determining the redox state of Fe from *L*- and *M*-edge spectra requires high vacuum conditions, which limits the field of application of the method. Despite their low intensity and low intrinsic resolution, XANES spectra at Fe-*K* edge (corresponding to the quadripolar 1s → 3d transitions for which intrinsic core-hole lifetime broadening is 3–4 times higher than for *L*-level transitions), are used to provide information on the local coordination environment for a wide variety of Fe- and transition element-bearing phases under in situ varying temperature and pressure conditions (Wilke et al. 2001; Farges et al. 2001a, 2001b for Ni).

In addition, the methods listed above to determine the $Fe^{3+}/\Sigma Fe$ ratios may require specific types of sample preparation, plus their use is often restricted by limited accessibility to the instrumental setting. The method described herein utilizes the electron microprobe, a basic instrument widespread in mineralogy and petrology, which is well known to provide chemical analyses in an automated mode of micrometer-sized areas over the full cm^2-sized surfaces of standard thin sections. This ability to process routinely large samples after only minimal preparation (the mechanical polishing at the micrometer level of the surface is just required for the thin section) is definitely a great advantage of the electron microprobe over other micro- and nano-beam methods of elemental analysis, including the speciation of Fe (e.g., Fialin et al. 2001 and references therein; Höfer et al. 1994, 2000).

Theoretical Background: Mechanisms for Self-Absorption-Induced Shift of the Fe*L*α Peak

For the electron microprobe, the oxidation state of Fe can be related to the self-absorption-induced shift toward lower energy of the Fe*L*α emission peak ($3d \rightarrow 2p_{3/2}$ radiative transition) (Fialin et al. 2001). The strongly absorbing Fe-L_3-edge XANES are involved in the self-absorption mechanism of part of the Fe*L*α photons generated in a bulk insulating or semi-conducting material. Indeed, the so-called lifetime effects, dominated by several broadening and shift mechanisms of the atomic levels generated by the $2p_{3/2}$ core-hole state (deGroot 1994 and references therein), are the origin of substantial overlap of the Fe*L*α emission band with the Fe-L_3-edge XANES in the region of the Fermi level.

Core-hole effect

The interaction between a core electron and an incoming particle produces an increase of the intra-atomic potential due to the creation of an electron-hole system. This perturbation is accompanied by a relaxation of the system leading the atomic levels being pulled down toward higher binding energies by an amount called the relaxation energy (Bonnelle 1987). For ionization processes in which the ejected electron is promoted far into the conduction band, which is composed of admixtures of extended empty states, the electron and the hole are dissociated and the relaxation energy is maximum. In metallic compounds the core hole is rapidly screened by valence electrons, which minimizes the intra-atomic relaxation energy. In oxides and silicates the core hole screening occurs through valence electron transfers from adjacent ligands. A fair illustration of the strength of the relaxation energy was recently given by X-ray photoelectron spectroscopy (XPS) spectra recorded from α-Fe_2O_3 (Droubay and Chambers 2001). In the latter oxide, the 2p levels were found to be shifted by about 9 eV toward higher binding energies when the core hole is unscreened (corresponding to the $2p^53d^5$ configuration for the Fe^{3+} ions) compared to the situation where the core hole is "well-screened" by valence electrons ($2p^53d^6\underline{L}$ configuration where $\underline{L}$ denotes an O 2p ligand hole.

In an excited state, both electron and hole remain in Coulomb interaction and the core hole is partially screened by the electron, leading to reduced (but not zero) relaxation energy. In fact, all filled and empty atomic levels are shifted to about the same relaxation energy as a consequence of the presence of the core hole (in contrast to band-like levels, including the metal 4 sp empty band and the O atom 2p filled band for transition-metal-bearing silicates, which are weakly shifted). Consequently, the relaxation energy is not observable from 2p emission bands because the core hole is present in the initial state of the ionization process ($2p^53d^N$ configuration, with $N = 5$ for Fe^{3+} and $N = 6$ for Fe^{2+}), and hence transitions occur from two equally shifted atomic levels. This insensitivity to the core hole effect for the position of emission bands was demonstrated recently for the Mn$K\beta_{1,3}$ emission band ($3p \rightarrow 1s$ radiative transition) in MnO (Glatzel et al. 2001). Calculated XPS spectra predicted a shift of ≈6.8 eV toward higher binding energies for the 1s level when the 1s core hole is unscreened compared to the screened hole event, whereas corresponding calculated $K\beta_{1,3}$ spectra were found to have a separation of only a few tenths of an eV.

In contrast, for absorption the core hole is present in the final state of the excitation process ($2p^53d^{N+1}$ configuration), and so the energy necessary to create the core hole is reduced (the atomic-like empty 3d levels are pulled down during the lifetime of the core hole), which causes the absorption spectra to be shifted toward lower energies. The core-hole-induced shift can be as large as 2 eV, as reported by deGroot et al. (1990) for 3d transition-metal fluorides. Similar shifts have been reported for the *K*- and $L_{2,3}$-ELNES edges of Mg in MgO and Al in Al_2O_3 (Mo and Ching 2000). For comparison, d-d optical transitions can be probed in the UV-visible-IR region (400–2500 nm) for silicates (refer Burns 1993 for a complete review of these absorption processes), which gives energy gaps between filled and empty 3d levels typically below 3 eV. In summary, the core hole has just an effect of lifetime broadening on the emission bands (Lorentzian broadening with up to 0.5 eV full width at half maximum for 3d transition metals, Hanzely and Liefeld 1971), whereas it is also responsible for a noticeable energy shift of the absorption bands, leading both emission and absorption bands to overlap partially.

Satellite emissions

The Fe*L*α emission band is also composed of a satellite emission band emitted from multiply ionized atoms. Two types of processes can lead to multiple-vacancy states: Auger and Coster-Kronig (CK) transitions in the singly ionized state, which leave the atom with an extra vacancy, and shake-off and shake-up processes, which induce the simultaneous ejection of two electrons during the inelastic collision with the incident

particle. When the incident electrons have energies in the range between the L_{II}-state threshold and about three times that amount, the high energy side of the diagram band (i.e., the normal band emitted from singly ionized atoms) becomes distorted by the progressive development of these satellite emissions. Because the beam energies employed with the microprobe are well in excess of the FeL_{II} threshold (typically 5–20 keV in routine use, to be compared to 721 eV for the FeL_{II} threshold), the satellite band may reach some tens of percent of the diagram band intensity. The shake-off and shake-up satellite band lie within 2–5 eV from the Fe$L\alpha$ diagram band maximum (Eisebitt et al. 1994). In addition, CK satellites (particularly the L_2-$L_3M_{4,5}$ transition) may contribute to a large part to the diagram band intensity (Hague et al. 1995).

Self-absorption of the Fe$L\alpha$ photons of higher energy emitted in both diagram and satellite (non diagram) bands causes large asymmetries on the high energy side of the Fe$L\alpha$ peak, leading to peak position shifts (Rémond et al. 1996).

In addition, many studies performed on silicates and glasses (e.g., Cressey et al. 1993; Henderson et al. 1995) have shown that the 2p absorption spectra of Fe^{2+} are systematically shifted toward lower energy (c.a. 1.5–1.6 eV) relative to Fe^{3+}. In comparison, the 2p emission bands for both Fe ions are less separated. This feature is illustrated in Figure 1a, which shows that the shift in energy is reduced to 0.21 eV for both (self-absorption-free) $L\alpha$ peaks emitted from an almandine (pure Fe^{2+}-bearing garnet) and an andradite (pure Fe^{3+}-bearing garnet). Due to self-absorption effects, the Fe$L\alpha$ peak shift for both minerals is enlarged to 1.2 eV for 15 keV beam energy. Figure 1b gives a better sense of the actual Fe^{2+} and Fe^{3+} peak shapes for both minerals. Such a large energy shift for absorption bands compared to emission bands is reflected as more overlap for both Fe^{2+} emission and XANES-absorption bands. Higher self-absorption effects are thus expected for Fe^{2+}-bearing compounds. For mixed Fe^{2+}-Fe^{3+}-bearing compounds, self-absorption at Fe^{2+} sites is responsible for most of the Fe$L\alpha$ peak shift toward lower energy. This difference in self absorption effects on both Fe^{2+} and Fe^{3+} $L\alpha$ peak positions is the primary physical property upon which is based the current method for determining $Fe^{3+}/\Sigma Fe$.

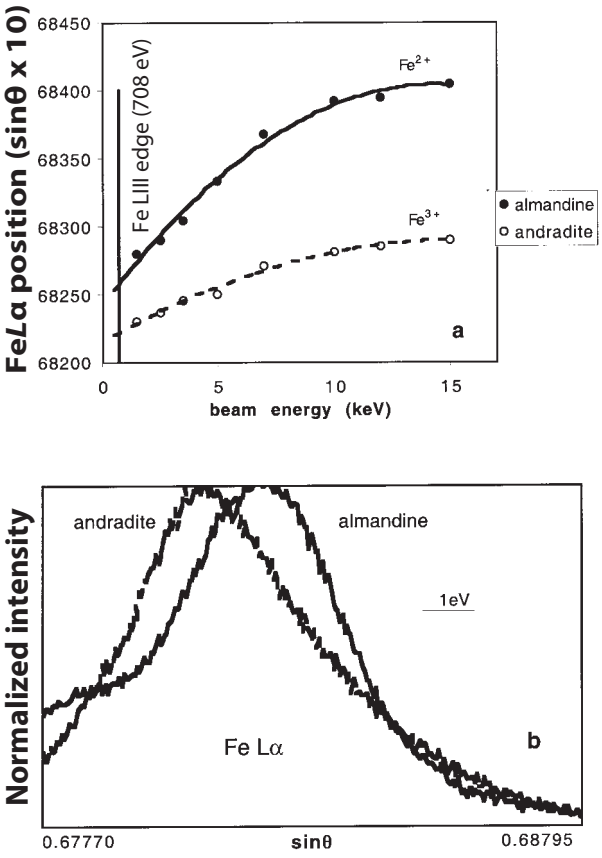

FIGURE 1. (**a**) Evolution of the Fe$L\alpha$ peak maximum (expressed as the Bragg angle sinθ measured with a TAP monochromator) as a function of the beam energy, for an almandine (pure Fe^{2+}-bearing garnet) and an andradite (pure Fe^{3+}-bearing garnet). The beam energy was varied from 2.5 to 15 keV. The self absorption increases with increasing beam voltage, which shifts the Fe$L\alpha$ peak toward longer sinθ (i.e., lower energies). This phenomenon is particularly visible for Fe^{2+}. The values extrapolated (by second-order polynomial fits) to the position of the Fe L_{III} edge give an estimation of the actual (i.e., the self-absorption free) peak positions. The actual Fe^{2+} $L\alpha$ peak position is found to be shifted by 0.21 eV toward lower energies compared to Fe^{3+} $L\alpha$. (**b**) 15 keV wavelength scan profiles showing the shift in maximum position (≈1.2eV) between the almandine $Fe^{2+}L\alpha$ peak and the andradite $Fe^{3+}L\alpha$ peak.

DESCRIPTION OF THE METHOD, CAPABILITIES, AND LIMITATIONS

Methodology for measuring the Fe$L\alpha$ peak position

In our experiments, the peak positions were determined by using the peak search routine available on the electron microprobe of the study (Cameca PC-controlled-SX100 type). A first maximum value of the peak is measured by sampling the signal over an enlarged wavelength range around the theoretical peak position. The approached peak position is then refined after the wavelength range is reduced and the intensity samples fitted with a gaussian function. The experimental peak position is the average of data collected from two wavelength dispersive spectrometers equipped with TAP monochromators. The time required for a single peak search is 30 s. The precision of the measurements is improved by using the average of accumulated peak search runs. Given the sensitivity of glasses to prolonged beam exposure (described below), the experimental protocol should be established as a trade-off between (1) limiting beam damage (both low beam power and short time for data collection) and (2) measuring $Fe^{3+}/\Sigma Fe$ with acceptable precision (high beam power and long time for data collection). The following operating conditions have been established for a suite of 20 glasses with 6-9 wt% Fe (see full composition in Table 1 of Fialin et al. 2001), used as reference materials to validate the method: 15 keV, 240 nA, and 20–30 μm beam, 60 accumulated peak search runs (for a total time of 30 min).

Construction of working curves

In addition to the oxidation number of Fe, the self-absorption induced shift of the Fe$L\alpha$ peak is dependent on other characteristics of the bulk matrix, namely the total Fe concentration (self-absorption increases with the total Fe concentration) and, to

a lesser extent for common silicates and glasses, the density (or the mean atomic number) and the absorption of Fe$L\alpha$ by other elements. Figure 2 shows the evolution at 15 keV beam energy of the $Fe^{2+}L\alpha$ and $Fe^{3+}L\alpha$ peak positions (expressed as the sine of the Bragg angle, $\sin\theta_{Fe2+}$ or $\sin\theta_{Fe3+}$, of the $L\alpha$ peak measured with a TAP monochromator) as a function of the total wt% Fe for a series of pure Fe^{2+}- and pure Fe^{3+}-bearing silicates. Within the 5–20 wt% Fe range, experimental plots (reprinted from Fialin et al. 2001) can be fitted by low-order polynomials, showing similar behavior as in Figure 1a for both $Fe^{2+}L\alpha$ and $Fe^{3+}L\alpha$ peak positions with increasing self-absorption conditions. The parabolic and linear fits in Figure 2 are suited to express further working curves under quite simple mathematical forms. The evolution of the offset between the Fe^{2+} and Fe^{3+} peak positions, deduced from the difference between both Fe^{2+} and Fe^{3+} fits of Figure 2, can be written:

$$y = 0.355x^2 - 14.716x + 27.339 \quad (1)$$

where $y = \sin\theta_{Fe3+} - \sin\theta_{Fe2+}$ and x is the Fe wt% concentration.

This offset is close to 40 sinθ increments (1 increment = 10^{-5} sinθ) for 5 wt% Fe, enlarged to 125 sinθ increments for 20 wt% Fe. Such quite large Fe^{2+}-Fe^{3+} intervals allow the Fe$L\alpha$ peak position to be easily traced for varying $Fe^{3+}/\Sigma Fe$ in mixed Fe^{2+}-Fe^{3+} compounds. For an unknown, the position of the Fe$L\alpha$ peak, $\sin\theta_X$, is localized relative to the relevant Fe^{2+} end-member positions (i.e., $\sin\theta_{Fe2+}$ corresponding to the total Fe concentration of the unknown, as deduced from the reference Fe^{2+} curves of Fig. 2). To prevent any discrepancy due to mechanical drift with time of the analyzing spectrometers, $\sin\theta_X$ was always scaled to the Fe$L\alpha$ peak position for hematite (referred to as $\sin\theta_{Fe2O3}$). Accordingly, the required offset, $(\sin\theta_X - \sin\theta_{Fe2+})$, can be written $(\sin\theta_X - \sin\theta_{Fe2O3}) + (\sin\theta_{Fe2O3} - \sin\theta_{Fe2+})$. The term in the second parenthesis can be expressed relative to the total Fe concentration for the reference silicate series:

$$y = 0.335x^2 - 15.869x + 159.41 \quad (2)$$

Using the above working curves (Eqs. 1 and 2) and the measured offset, $(\sin\theta_X - \sin\theta_{Fe2O3})$, gives the relative peak position

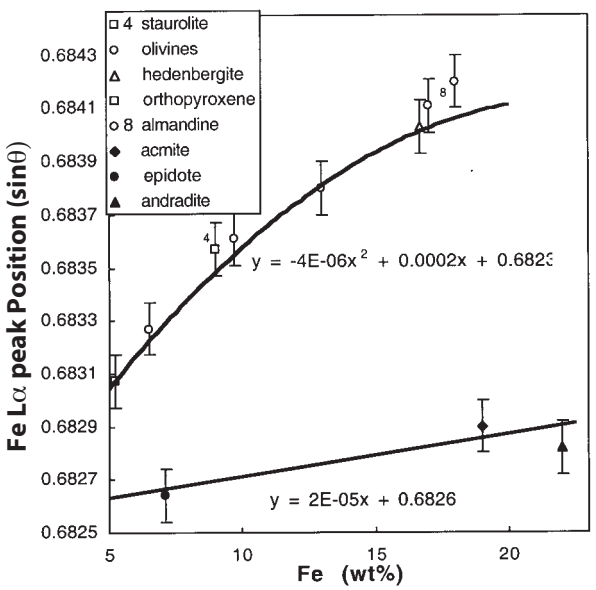

FIGURE 2. Variations of the Fe$L\alpha$ peak position measured at 15 keV with a TAP monochromator as a function of the total Fe concentration (5–20 wt% Fe) for a series of pure Fe^{2+}-bearing and pure Fe^{3+}-bearing silicates (plots are partially reprinted from Fig. 3 in Fialin et al. 2001). Numbers next to symbols in the legend indicate coordination numbers of Fe ions for minerals in which coordination numbers are not six. First- and second-order polynomial fits are shown.

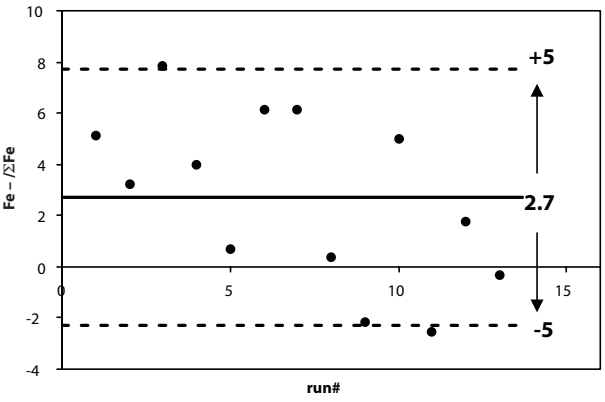

FIGURE 3. $Fe^{3+}/\Sigma Fe$ measured from a San Carlos olivine with 7.4 wt% Fe. Operating conditions: 15 keV, 240 nA, 20 µm, 60 peak searches integrated per plot (30 min acquisition). This result, namely $Fe^{3+}/\Sigma Fe = 2.7 \pm 5\%$ (2σ precision), can be taken as a measure of the intrinsic accuracy and precision expected for the series of reference glasses (with Fe concentration ranging from 6 to 9 wt%) of this study.

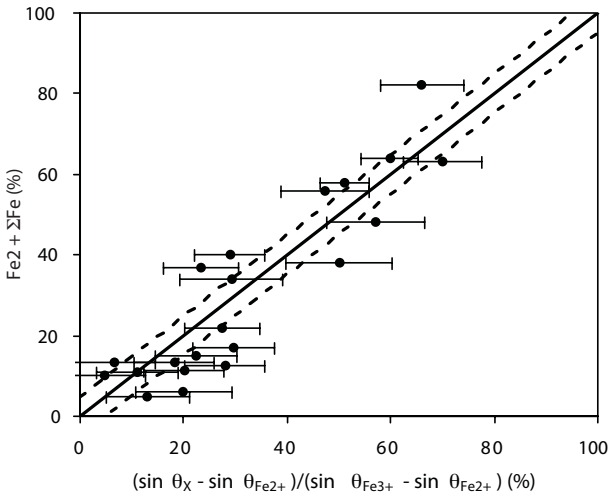

FIGURE 4. Nominal/measured $Fe^{3+}/\Sigma Fe$ for the series of reference glasses. For each plot, error bars on the x-axis correspond to the uncertainty found for the Fe$L\alpha$ peak position after 60 peak searches performed on 60 fresh surfaces of the specimen. The error bar length is generally in excess of the expected ±5% interval (shown by the dashed lines on either side of the 1:1 line) measured for the San Carlos olivine. These results may denote inhomogeneities of $Fe^{3+}/\Sigma Fe$ at the scale of a few tens of micrometers. Same operating conditions as Figure 3.

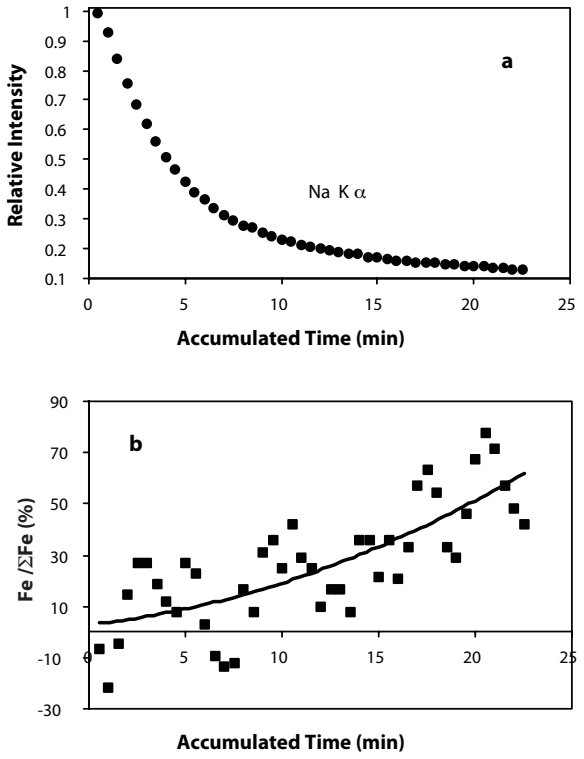

FIGURE 5. (**a**) Time-dependent loss of the Na*K*α intensity (measured with a TAP monochromator) within 20–25 min irradiation time for a reduced basaltic glass [with major-element composition (in wt%): MgO=8.1, SiO_2=50.9, TiO_2=1.3, Al_2O_3=17.5, CaO=10.2, FeO_t=6.7, Na_2O=3.9]. 30s counting time per plot. Same beam conditions as Figure 4. (**b**) Beam-induced oxidation mechanism of the surface layer of the glass leading $Fe^{3+}/\Sigma Fe$ to increase from 6 to 60%. Plots represents 45 successive peak searches (30 s per peak search) performed on a single surface site. The scattering observed for the plots is representative of the average of four replicate series acquired at four different surface sites. No incubation period is appeared for the Na*K*α intensity loss kinetics indicating rapid migration of Na for this glass composition under the selected beam conditions. In contrast, the oxidation mechanism, involving electron transfer from Fe^{2+} cations to O atoms left in excess by the removal of Na^+, is obviously slower.

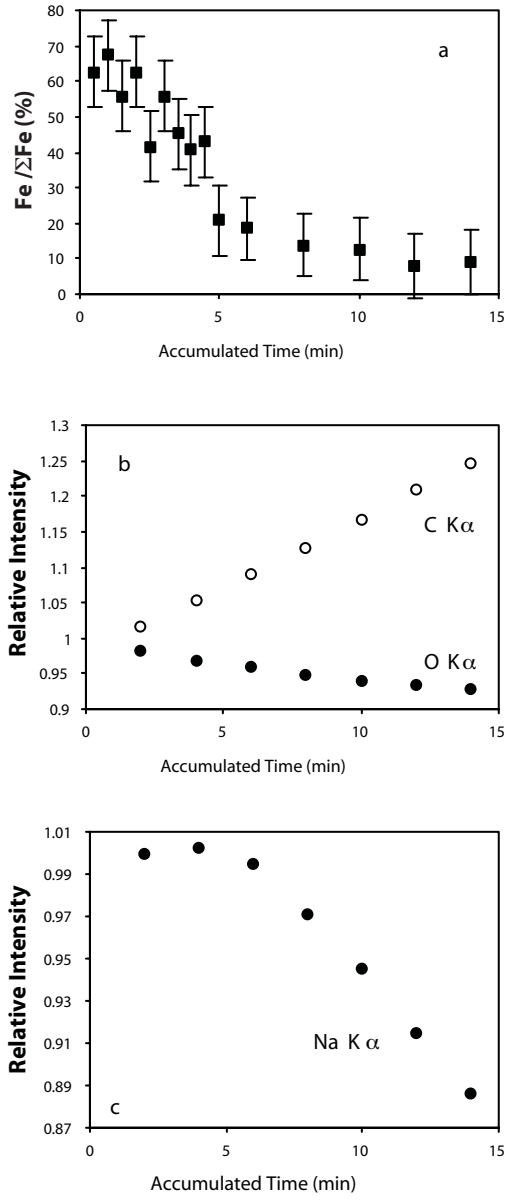

FIGURE 6. (**a**) Reduction kinetics for a mixed Fe^{2+}-Fe^{3+} glass [major-element composition (in wt%): MgO = 9.9, SiO_2 = 52.9, CaO = 16.9, FeO_t = 12.6, Na_2O = 5.9] whose $Fe^{3+}/\Sigma Fe$ decreases from 65 to less than 10% within 15 min irradiation time (same beam conditions as Fig. 4 excepted 30μm spot diameter). Plots above (resp. below) 5 min result from peak searches of 2 min (resp 30s), and they are the average of three (resp. ten) replicate measurements at three (ten) fresh surface sites. (**b**) Time-dependent evolution of the O*K*α intensity (measured with a W/Si metallic multilayer monochromator, or MMM, with $2d$ = 6nm) and the C*K*α intensity (measured with a Ni/C MMM with $2d$ = 9.5nm). These plots show that the reduction of the surface layer is not related to the removal of oxygen atoms. The loss of O*K*α intensity is correlated with the carbon contamination build-up due to cracking of pump oil molecules present in the sample chamber. 2 min counting time per plot. (**c**) Time-dependent loss of Na*K*α intensity showing that the reduction mechanism occurs during the incubation period of Na.

for the unknown $(\sin\theta_X - \sin\theta_{Fe^{2+}})/(\sin\theta_{Fe^{3+}} - \sin\theta_{Fe^{2+}})$. The last parameter is taken as the measured $Fe^{3+}/\Sigma Fe$.

An important result deduced from Figure 2 is the insensitivity of the Fe*L*α peak position to the geometry of the Fe sites for pure Fe^{2+}-bearing and pure Fe^{3+}-bearing minerals. One can thus assume that measurements performed on synthetic reference glasses with $Fe^{3+}/\Sigma Fe \cong 0\%$ and $Fe^{3+}/\Sigma Fe \cong 100\%$ (not available for this study) would match the data from minerals presented in Figure 2 (a further justification of this point is presented below). It should be pointed out that these working curves are specific to the microprobe used. These curves may be vary somewhat from one microprobe to another, depending on the quality of the spectrometer for which any bias in the linear focusing geometry (misadjustment on the Rowland circle of the probe-monochromator-detector system in particular) is reflected as lost resolution. In addition, substantial loss of resolution is noted when the probe is

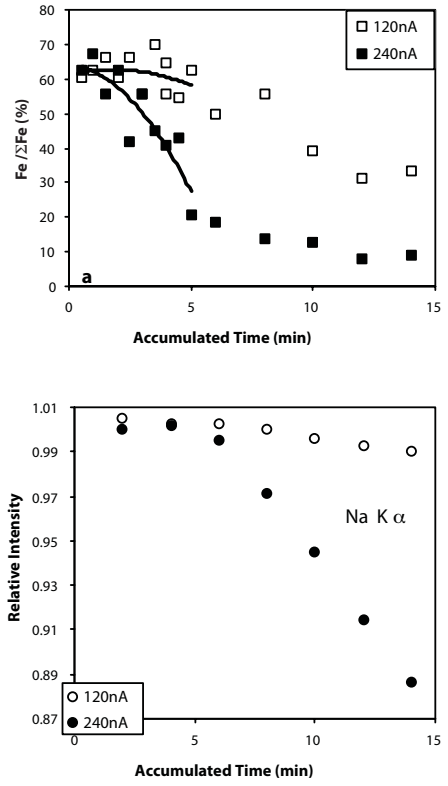

FIGURE 7. Comparison of reduction kinetics (**a**) for two beam current intensities (30 μm beam diameter for both). As expected, the reduction rate, as well as the Na migration shown in (**b**), is reduced at lower current. Parabolic fits applied to plots acquired below 5 min give consistent zero-time values for $Fe^{3+}/\Sigma Fe$. Same operating conditions as Figure 6.

no longer regarded as a point source (typically over 40–50 μm for the microprobe of the study).

Accuracy and precision

Figure 3 gives a realistic approach of the intrinsic accuracy and statistical precision expected for the method through the example of a San Carlos olivine (a mineral with 7.4 wt% Fe, which is a median value of the investigated 6–9 wt% Fe range) for which $Fe^{3+}/\Sigma Fe$ was measured to 2.7±5% (2σ precision) by application of the working curves under the operating conditions given in the previous section. The systematic offset of 2.7% found for olivine (a mineral well known to have essentially $Fe^{3+}/\Sigma Fe = 0$) is relatively small and acceptable in view of the precision of ± 5% absolute achieved for the measurements. The 6–9 wt% Fe range is suited for the study of a large variety of natural glasses. However, glasses with Fe concentrations below 6 wt% are common and, in theory, can be processed by the present method, provided that the Fe concentrations are high enough to produce detectable Fe*L*α peaks. Preliminary measurements performed on some of the glasses with low Fe concentrations have led to large discrepancies in the measured $Fe^{3+}/\Sigma Fe$ using the fitting curves constructed for this study. This demonstrates the need for pure Fe^{2+}-bearing and pure Fe^{3+}-bearing reference materials, although these materials are not easy to find in the required Fe concentration range (2–6 wt% Fe), especially for Fe^{3+}.

Results for the suite of reference glasses are presented in Figure 4 where nominal $Fe^{3+}/\Sigma Fe$ values (measured by wet chemistry) are plotted against measured values. Despite obvious scattering and error bars larger than the expected ±5% error limits for the statistical precision, plots are aligned along the 1:1 line. This result shows, *a posteriori*, that the fitting curves in Figure 2 (constructed with data from pure Fe^{2+}-bearing and pure Fe^{3+}-bearing silicate minerals) are applicable to glasses. A major source of discrepancies is the formation of Fe clusters randomly dispersed in glasses (Bingham et al. 1999). A varying proportion of Fe clusters in the probed volume should be reflected as the Fe*L*α peak shifts as a result of local changes in both $Fe^{3+}/\Sigma Fe$ ratios and total Fe concentrations. We suggest that discrepancies noted in Figure 4 may be caused by inhomogeneities in iron cluster distribution at the scale of few micrometers to few millimeters: (1) the millimetric reference glass sample picked up from the batch used for chemical analyses may exhibit some changes compared to the average composition; or (2) for individual specimens, compositional changes could be revealed as each of the 60 peak searches were acquired from a fresh surface site to limit beam damage (see next section). Unexpected beam damage caused disagreement between nominal and measured values for a first series of measurements performed on these reference glasses (see Fig. 4a in Fialin et al. 2001). Bingham et al. (1999) also noted that clustering in glasses is accompanied by intervalence charge transfers (IVCT) between adjacent Fe^{2+} and Fe^{3+} sites. As previously reported (Fialin et al. 2001), IVCT may strongly influence the Fe*L*α peak position, especially when Fe^{2+} and Fe^{3+} sites have similar symmetries. For glasses, Fe may be distributed over four distinct site geometries (Brown et al. 1995), which potentially limit the IVCT effects (i.e., the Fe*L*α peak is shifted toward shorter wavelength leading $Fe^{3+}/\Sigma Fe$ to be measured in excess relative to the nominal value). No such IVCT effects are revealed in Figure 4.

Beam-induced oxidation-reduction mechanisms of glasses

The migration of mobile ions (alkalis) inside the excitation volume is the most common and documented beam damage effect occurring in glasses exposed to electron bombardment (Morgan and London 1996 and references therein). The role of the electric field present in the charged excitation volume has been clearly established for this migration process (e.g., Jbara et al. 1995). The time-dependent loss of Na*K*α intensity is illustrated in Figure 5a for a basaltic glass with 3.9 wt% Na_2O. For reduced glasses, the Na^+ diffusion toward the bulk is expected to cause oxidation of the surface by increase of the O atom/cation ratio (i.e., not by addition of environmental O atom present in the specimen chamber under residual pressure). This oxidation mechanism causes the Fe*L*α peak to shift toward lower wavelength (i.e., toward the Fe^{3+}*L*α reference end-member position for the unknown composition), with subsequent increase of $Fe^{3+}/\Sigma Fe$ (Fig. 5b). For a beam power of 15 keV, 240 nA, and with a 20 μm diameter spot, $Fe^{3+}/\Sigma Fe$ increase from 3% (the nominal value determined by wet chemistry is 6%) to 60% during 45 peak searches performed at the same surface site (20–25 min accumulated time). The migration rate of Na is higher than that of the oxidation mechanism involving electron transfers from Fe^{2+} to the O atoms left in excess by the

removal of Na^+. Indeed, the removal of two Na^+ leaves one non-bridging O atom (as O^-) that combines with two adjacent FeO to give Fe_2O_3. The Na migration/oxidation rate ratio is thus at least two. In addition, the close vicinity of the non-bridging O atom and FeO is required for oxidation (another product of Na migration is the creation of O_2^{2-} molecular ions between two adjacent non-bridging O atoms); the lower the Fe atomic fraction in the glass, the slower the oxidation. For this example the oxidation kinetics are slow enough to allow the use of a parabolic fit to recover consistent "zero time" $Fe^{3+}/\Sigma Fe$ values (the starting Na migration/oxidation rate ratio is about 25).

Figure 6a shows the kinetics of reduction for an Fe^{2+}- and Fe^{3+}-bearing glass whose $Fe^{3+}/\Sigma Fe$ decreases from 65% to less than 10% during 15 min irradiation time with a 15 keV, 240 nA, and 30 μm beam. Reduction is not related to the removal of O atoms (e.g., by desorption), as it is demonstrated in Figure 6b; the observed time-dependent loss of O*K*α intensity is caused by the increase of the carbon contamination deposited near to the spot by cracking of pump oil molecules present in the specimen chamber. Indeed, O*K*α is highly absorbed by carbon and the intensity gently decreases as the contamination layer builds up. In addition, reduction occurs during the period where no significant Na migration occurs (the plateau region shown in the initial few minutes of the curve in Figure 6c is called "incubation" period), i.e., where the glass composition remains stable. Glass reduction, as well as numerous mechanisms of defect formation in solid at low incident energies, may occur through the production and decay of electronic excitation. Under irradiation with photons or charged particles, excitonic states are created in semiconducting and insulating materials (see, e.g., Itoh and Stoneham 2001 for a discussion of these mechanisms). These states, also known as excitons, consist of electron-hole (e^--h^+) pairs with energies just below the bandgap width of the material (~9 eV for glasses). Most e^--h^+ pairs generated are unstable and recombine in picoseconds (the released energy is generally dissipated as heating of the glassy lattice). However, some of these pairs may be trapped on particular sites of the lattice (defect sites), leading to the creation of point defects. Several electron and hole traps have been identified in glasses (Boizot et al. 1998, 2001). In particular, the latter authors have shown that Fe^{3+} ions act as electron traps during X-ray and electron irradiation. The electron component of an exciton can be attracted by the potential well formed at a Fe^{3+} site, which results in glass reduction ($Fe^{2+} + e^- \rightarrow Fe^{3+}$). After a short incubation period (less than ~1 min, as deduced from plots in Fig. 6a), the reduction mechanism is started. After the Na incubation period (~5 min) the reduction rate may slowed to some extent by the concurrent oxidation related to the migration of Na^+. Reducing the beam current to 120 nA (1) stops the Na migration (intensity loss reduced to less than 1% after 15 min irradiation) and (2) increases the incubation period to few minutes as well as decreases the diffusion rate for electrons (Fig. 7). For both beam currents (120 and 240 nA) parabolic fits to plots acquired within the initial 5 min give consistent zero-time values for $Fe^{3+}/\Sigma Fe$.

The above results show the need to operate with beam current densities as low as possible. Such reduced excitation conditions should be balanced by enhanced sensitivity of the detection system to keep the time required for the measurement of the peak position constant with unchanged precision (see below for a description of some promising developments on X-ray optics).

Technological developments

For beam sensitive glasses, such as silica-rich glasses or hydrous glasses (Morgan and London 1996), more moderate beam conditions should be adopted to increase the incubation period, with the intent of modeling the early variations of the peak position with improved accuracy. The counterpart to reduction of beam power is increased statistical error in the measurement of the peak position. The easiest way to overcome this difficulty is to increase the 60 required peak searches (doubling this number would reduce the error on $Fe^{3+}/\Sigma Fe$ to ca. ± 3.5% instead of ±5%), which requires that the sample be large enough to obtain the required number of fresh surfaces. However, one of the main advantages of the method, i.e., measuring $Fe^{3+}/\Sigma Fe$ at a scale of few tens of micrometers, may then cancel. Another way is to improve the sensitivity of the microprobe. For this purpose, a first technological solution would be to increase the dimensions of the TAP monochromator to collect the X-ray flux within a larger solid angle. This type of enlarged TAP is now available with dimensions 60 × 22 mm^2 (instead of 32 × 22 mm^2 for the regular TAP) and mounted according to the "exact focusing" Johansson geometry (instead of the Johann geometry for the regular TAP). When the monochromator surface is quite large, the two ends of the crystal are out of the Rowland circle for the Johann geometry, leading to loss in resolution. Resolution can be recovered with the Johansson geometry in which the angle of incidence is constant for all points in the plane of the Rowland circle. Enlarged TAP has been recently tested at the Cameca lab (Pierre-François Staub, personal communication) showing reflectivities increased by a factor 3 for the Fe*L*α peak with no loss in resolution compared to the regular TAP (namely FWHM ~5eV). A second possibility is to replace the poorly reflecting TAP monochromator by a metallic multilayer monochromator (MMM) especially designed for the detection of Fe*L*α. A recent study on a new generation of etched MMM (also known as lamellar multilayer amplitude gratings, or LMAG) has described a promising Mo/Si-based structure offering similar resolving power as TAP for peaks with energies on the order of 1 keV (André et al. 2001). Further technological refinements, including the etching of the grating with a 1 μm period (compared to the 15 μm period of the current LMAG), would increase the reflectivity by a factor of at least 10 for the LMAG compared to the regular TAP. High reflectivity and high resolution devices have also been described based on the concept of multi-stepped pseudo-spherical diffractor (Marcelli et al. 1998). For this technology, the surface of the monochromator crystal holder is designed and machined to optimize resolution and reflected intensity. Gain on resolution of about one order of magnitude can be achieved compared to conventional cylindrically bent monochromators. Improving resolution to such an extent should produce sharper peaks with consequent better accuracy in the measurement of the Fe*L*α peak position.

Concluding remarks

The results of this study show the capability of the electron microprobe to give consistent measurements of the $Fe^{3+}/\Sigma Fe$

ratios for glasses with total Fe concentrations above 5 wt%. The method consists of processing the Fe$L\alpha$ peak position by a series of working curves constructed from reference materials (minerals). For glasses with Fe concentrations between 6 and 9 wt%, the application of the protocol described herein leads to an uncertainty of ±5% absolute on $Fe^{3+}/\Sigma Fe$. On the one hand, the 60 peak searches required to obtain such an error should be acquired from glass surfaces as small as possible to keep the punctual analysis aspect of the method. On the other hand, the residence time of the electron spot (carrying a given current density) on a single surface site of the glass specimen should be adjusted to limit beam damage. Beam damage includes migration of Na^+ toward the bulk (leading to oxidation of a surface layer for reduced glasses) and excitonic mechanisms (leading to reduction of a surface layer for mixed Fe^{2+}-Fe^{3+} glasses). Such beam-induced oxidation-reduction mechanisms are controlled by the electric field generated by charging in the excitation volume. Movement of electrons from Fe^{2+} to O atoms (oxidation) or to Fe^{3+} (reduction) is thermally activated after an incubation period that should be ideally higher or equal to the time required for the measurement of $Fe^{3+}/\Sigma Fe$. At least the evolution of the measured $Fe^{3+}/\Sigma Fe$ due to beam damage should be easily traced (e.g., by linear or parabolic fits to experimental data) during the measurement time. Reducing beam damage requires: (1) low beam current density (i.e., beam current below 240 nA and/or probe diameter above 20–30 μm for the present protocol), and (2) short time per $Fe^{3+}/\Sigma Fe$ analysis (currently ~30 min). Both requirements are generally not applicable to small areas due to lack of precision and accuracy for the measured data. The development of new X-ray optics, such as those reported above in the text, would soon bring solutions to this problem. Determining $Fe^{3+}/\Sigma Fe$ in basaltic glasses trapped as melt inclusions in phenocrysts is one of the main fields of application of this method. Melt inclusions enable, for instance, determination of the O atom fugacity at various stages in the evolution of magmatic systems, on the basis of the $Fe^{3+}/\Sigma Fe$ ratios (e.g., Danyushevsky et al. 2002). Unfortunately, the method is still useless for glasses with Fe concentrations below 5 wt%, due to a lack of reference specimens (especially pure Fe^{3+}-bearing specimens to construct similar working curves as in Fig. 2).

ACKNOWLEDGMENTS

The authors thank M. Wilke, Institut für Geowissenschaften Universität Postdam (GER), whose suggestions enhanced the quality of the manuscript. B. Boizot (Laboratoire des solides irradiés, Ecole Polytechnique-CEA, Palaiseau) is greatly acknowledged to have drawn our attention into his published works on irradiation induced reduction of glasses, as well as for further fruitful discussions on this subject.

REFERENCES CITED

Amthauer, G. (1996) Ligand field theory and inter- and intracrystalline cation distribution of transition elements in minerals and related inorganic compounds. Physics and Chemistry of Minerals, 23, 276–283.

André, J.M., Benbalagh, R., Barchewitz, R., Ravet, M.F., Raynal, A., Delmotte, F., Bridou, F., Julie, G., Bosseboeuf, A., Laval, R., Soullié, G., Rémond, C., and Fialin, M. (2001) Soft-X-ray multilayer monochromator with improved resolution and low specular background. X-ray spectrometry, 30, 212–215.

Bingham, P.A., Parker, J.M., Searle, T., Williams, J.M., and Fyles, K. (1999) Redox and clustering of iron in silicate glasses. Journal of Non-Crystalline Solids, 253, 203–209.

Boizot, B., Petite, G., Ghaleb, D., and Calas, G. (1998) Radiation induced paramagnetic centres in nuclear glasses by EPR spectroscopy. Nuclear Instruments and Methods in Physics Research, B141, 580–584.

——— (2001) Dose, dose rate and irradiation temperature effects in β-irradiated simplified nuclear waste glasses by EPR spectroscopy. Journal of Non-Crystalline Solids, 283, 179–185.

Bonnelle, C. (1987) X-ray spectroscopy. Annual Report C, p. 201–272. The Royal Society of Chemistry, London.

Brown, G.E. Jr., Farges, F., and Calas, G. (1995) Structure, Dynamics, and Properties of Silicates Melts. In J.F. Stebbins, D.B. Dingwell, and P.F. McMillan, Eds., Stucture, Dynamics and Properties of Silicate Melts, 32, 31–410. Reviews in Mineralogy, Mineralogical Society of America, Washington, D.C.

Burns, R.G. (1993). Mineralogical applications of crystal field theory, second edition. In A. Putnis and R.C. Liebermann, Eds., Cambridge topics in mineral physics and chemistry, vol. 5. Cambridge University Press, U.K.

Cressey, G., Henderson, C.M.B., and van der Laan, G. (1993) Use of L-edge X-ray absorption spectroscopy to characterize multiple valence states of 3d transition metals; a new probe for mineralogical and geochemical research. Physics and Chemistry of Minerals, 20, 111–119.

Danyushevsky, L.V., McNeill, A.W., and Sobolev, A.V. (2002) Experimental and petrological studies of melt inclusions in phenocrysts from mantle-derived magmas: an overview of techniques, advantages and complications. Chemical Geology, 183, 5–24.

Droubay, T. and Chambers, S.A. (2001) Surface-sensitive Fe 2p photoemission spectra for α-Fe_2O_3(0001): the influence of symmetry and crystal-field strength. Physical Review B, 64, 205414-1-6.

Eisebitt, S., Rubensson, J.E., Nicodemus, M., Böske, T., Blügel, S., Eberhardt, W., Radermacher, K., Mantl, S., and Bihlmayer, G. (1994) Electronic structure of buried α-$FeSi_2$ and β-$FeSi_2$ layers: Soft-X-ray-emission and -absorption studies compared to band-structure calculations. Physical Review B, 50-24, 18330–18340.

Farges, F., Brown, G.E. Jr., Petit, P.E., and Munoz, M. (2001a) Transition elements in water-bearing silicate glasses/melts. Part I. A high-resolution and anharmonic analysis of Ni coordination environments in crystals, glasses, and melts. Geochimica et Cosmochimica Acta, 65-10, 1665–1678.

Farges, F., Munoz, M., Siewert, R., Malavergne, V., Brown, G.E. Jr., Behrens, H., Nowak, M., and Petit, P.M. (2001b) Transition elements in water-bearing silicate glasses/melts. Part II. Ni in water-bearing glasses. Geochimica et Cosmochimica Acta, 65-10, 1679–1693.

Fialin, M., Wagner, C., Métrich, N., Humler, E., Galoisy, L., and Bézos, A. (2001) $Fe^{3+}/\Sigma Fe$ vs. FeLα peak energy for minerals and glasses: Recent advances with the electron microprobe. American Mineralogist, 86, 456–465.

Garvie, L.A.J. and Buseck, P.R. (1998) Ratios of ferrous to ferric iron from nanometre-sized areas in minerals. Nature, 396, 667–670.

Glatzel, P., Bergmann, U., de Groot, F.M.F., and Cramer, S.P. (2001) Influence of the core hole on Kβ emission following photoionozation or orbital electron capture: A comparison using MnO and $^{55}Fe_2O_3$. Physical Review B, 64, 045109-1-10.

deGroot, F.M.F. (1994) X-ray absorption and dichroism of transition metals and their compounds. Journal of Electron Spectroscopy and Related Phenomena, 67, 529–622.

deGroot, F.M.F., Fuggle, J.C., Thole, B.T., and Sawatzky, G.A. (1990) 2p X-ray absorption of 3d transition-metal compounds: An atomic multiplet description including the crystal field. Physical Review B, 42-9, 5459–5468.

Hague, C.F., Mariot, J.M., Guo, G.Y., Hricovini, K., and Krill, G. (1995) Coster-Kronig contributions to magnetic circular dichroism in the $L_{2,3}$ X-ray fluorescence of iron. Physical Review B, 51-2, 1370–1373.

Hanzely, S. and Liefeld, R.J. (1971) An L-series X-ray spectroscopic study of the valence bands in iron, cobalt, nickel, copper, and zinc. In L.H. Bennett, Ed., Electronic Density of States. National Bureau of Standards Special Publication 323, 319–327.

Henderson, C.M.B., Cressey, G., and Redfern, S.A.T. (1995) Geological applications of synchrotron radiation. Radiation Physics and Chemistry, 45-3, 459–481.

Höfer, H.E., Brey, G.P., Schulz-Dobrick, B., and Oberhänsli, R. (1994) The determination of the oxidation state of iron by the electron microprobe. European Journal of Mineralogy, 6, 407–418.

Höfer, H.E., Weinbruch, S., McCammon, C.A., and Brey, G.P. (2000) Comparison of two electron probe microanalysis techniques to determine ferric iron in synthetic wüstite samples. European Journal of Mineralogy, 12, 63–71.

Humler, E., Meyzen, C., Ludden, J., and Mevel, C. (1998) Geochemical variations in basaltic glasses from the South West Indian Ridge (49 to 69° E). AGU fall meeting, EOS 79, 878.

Itoh, C. and Stoneham, A.M. (2001) Materials modification by electronic excitation. Radiation Effects and Defects in Solids, 155 1-4, 277–290. Proceedings of the 14th International Conference on Defects in Insulating Materials, 3-7 April 2000, Johannesburg, South-Africa.

Jbara, O., Cazaux, J., and Trebbia, P. (1995) Sodium diffusion in glasses during electron irradiation. Journal of Applied Physics, 78, 868–875.

Marcelli, A., Soldatov, A.V., and Mazuritsky, M.I. (1998) Multistepped X-ray crystal diffractor based on a pseudo-spherical geometry. SPIE98 proceedings, 3448.

Mo, S.D. and Ching, W.Y. (2000) Ab initio calculation of the core-hole effect

in the electron energy-loss near-edge structure. Physical Review B, 62-12, 7901–7907.

Morgan VI, G.B. and London, D. (1996) Optimizing the electron microprobe analysis of hydrous alkali aluminosilicate glasses. American Mineralogist, 81, 1176–1185.

Petit, P.E., Farges, F., Wilke, M., and Solé, V.A. (2001) Determination of the iron oxidation state in Earth materials using XANES pre-edge information. Journal of Synchrotron Radiation, 8, 952–954.

Rémond, G., Gilles, C., Fialin, M., Rouer, O., Marinenko, R., Myklebust, R., and Newbury, D. (1996) Intensity measurement of wavelength dispersive X-ray emission bands: applications to the soft X-ray region. Mikrochimica Acta [Suppl.], 13, 61–86.

van Aken, P.A., Liebscher, B., and Styrsa, V.J. (1998) Quantitative determination of iron oxidation states in minerals using Fe $L_{2,3}$-edge electron energy-loss near-edge structure spectroscopy. Physics and Chemistry of Minerals, 25, 323–327.

van Aken, P.A., Styrsa, V.J., Liebscher, B., Woodland, A.B., and Redhammer, G.J. (1999) Microanalysis of $Fe^{3+}/\Sigma Fe$ in oxide and silicate minerals by investigation of electron energy-loss near-edge structures (ELNES) at the $M_{2,3}$ edge. Physics and Chemistry of Minerals, 26, 584–590.

Wilke, M., Farges, F., Petit, P.M., Brown, G.E. Jr., and Martin, F. (2001) Oxidation state and coordination of Fe in minerals: An Fe K-XANES spectroscopic study. American Mineralogist, 86, 714–730.

MANUSCRIPT RECEIVED MARCH 13, 2003
MANUSCRIPT ACCEPTED OCTOBER 23, 2003
MANUSCRIPT HANDLED BY MARC HIRSCHMANN